RF sputtered amorphous chalcogenide thin films for surface enhanced infrared absorption spectroscopy

F. Verger,[1,2] V. Nazabal,[1,*] F. Colas,[3] P. Němec,[2] C. Cardinaud,[4] E. Baudet,[1] R. Chahal,[1] E. Rinnert,[3] K. Boukerma,[3] I. Peron,[1] S. Deputier,[1] M. Guilloux-Viry,[1] J.P. Guin,[5] H. Lhermite,[6] A. Moreac,[7] C. Compère,[3] and B. Bureau[1]

[1]*Institut Sciences Chimiques de Rennes, UMR-CNRS 6226, Université de Rennes 1, 35042 Rennes cedex, France*
[2]*Department of Graphic Arts and Photophysics, Faculty of Chemical Technology, University of Pardubice, Studentska 573, 53210 Pardubice, Czech Republic*
[3]*IFREMER, Detection, Sensors and Measurements Laboratory, Technology Research and Development Department, 29280 Plouzané, France*
[4]*Institut des matériaux Jean Rouxel (IMN) UMR6502, Université de Nantes, CNRS, 44322 Nantes Cedex 3, France*
[5]*LARMAUR, Université de Rennes 1, Campus de Beaulieu, 35042 Rennes cedex, France*
[6]*IETR-Microélectronique, Université de Rennes 1, Campus de Beaulieu, 35042 Rennes cedex, France*
[7]*IPR, UMR-CNRS 6251 Université de Rennes 1, Campus de Beaulieu, 35042 Rennes cedex, France*
**virginie.nazabal@univ-rennes1.fr*

Abstract: The primary objective of this study is the development of transparent thin film materials in the IR enabling strong infrared absorption of organic compounds in the vicinity of metal nanoparticles by the surface plasmon effect. For developing these optical micro-sensors, hetero-structures combining gold nanoparticles and chalcogenide planar waveguides are fabricated and adequately characterized. Single As_2S_3 and $Ge_{25}Sb_{10}Se_{65}$ amorphous chalcogenide thin films are prepared by radio-frequency magnetron sputtering. For the fabrication of gold nanoparticles on a chalcogenide planar waveguide, direct current sputtering is employed. Fabricated single layers or hetero-structures are characterized using various techniques to investigate the influence of deposition parameters. The nanoparticles of gold are functionalized by a self-assembled monolayer of 4-nitrothiophenol. Finally, the surface enhanced infrared absorption spectra of 4-nitrothiophenol self-assembled on fabricated Au/Ge-Sb-Se thin films hetero-structures are measured and analyzed. This optical component presents a ~24 enhancement factor for the detection of NO_2 symmetric stretching vibration band of 4-nitrothiophenol at 1336 cm^{-1}.

OCIS codes: (300.6340) Spectroscopy, infrared; (310.1860) Deposition and fabrication; (310.6845) Thin film devices and applications; (160.2750) Glass and other amorphous materials; (280.4788) Optical sensing and sensors; (130.3060) Integrated optics: Infrared.

References

1. C. McDonagh, C. S. Burke, and B. D. MacCraith, "Optical chemical sensors," Chem. Rev. **108**(2), 400–422 (2008).
2. M. Zourob and A. Lakhtakia, *Optical Guided-wave Chemical and Biosensors I* (Springer, 2010).
3. B. H. Stuart, *Infrared Spectroscopy: Fundamentals and Applications* (Wiley, 2004).
4. K. Nishikida, E. Nishio, and R. W. Hannah, *Selected Applications of Modern FT-IR Techniques* (Kodansha, 1996).
5. A. Barth, "Infrared spectroscopy of proteins," Biochim. Biophys. Acta-Bioenergetics **1767**(9), 1073–1101 (2007).
6. B. B. Lahiri, S. Bagavathiappan, T. Jayakumar, and J. Philip, "Medical applications of infrared thermography: A review," Infrared Phys. Technol. **55**(4), 221–235 (2012).

#197051 - $15.00 USD Received 3 Sep 2013; revised 8 Nov 2013; accepted 15 Nov 2013; published 22 Nov 2013

7. K. D. Shepherd and M. G. Walsh, “Infrared spectroscopy - enabling an evidence-based diagnostic surveillance approach to agricultural and environmental management in developing countries,” J. Near Infrared Spec. **15**(2), 1–19 (2007).
8. R. H. Wilson and H. S. Tapp, “Mid-infrared spectroscopy for food analysis: recent new applications and relevant developments in sample presentation methods,” Trac-Trend. Anal. Chem. **18**, 85–93 (1999).
9. M. A. Schmidt, D. Y. Lei, L. Wondraczek, V. Nazabal, and S. A. Maier, “Hybrid nanoparticle-microcavity-based plasmonic nanosensors with improved detection resolution and extended remote-sensing ability,” Nat. Commun **3**, 1108 (2012).
10. B. J. Eggleton, B. Luther-Davies, and K. Richardson, “Chalcogenide photonics,” Nat. Photonics **5**, 141–148 (2011).
11. F. Charpentier, V. Nazabal, J. Troles, Q. Coulombier, L. Brilland, C. Boussard-Pledel, P. Nemec, H. Lhermite, J. Charrier, F. Smektala, M. Frumar, K. Le Pierres, N. Thybaud, and B. Bureau, “Infrared optical sensor for CO_2 detection,” in *Optical Sensors*, F. Baldini, J. Homola, and R. A. Lieberman, eds., vol. 7356, (SPIE, 2009), pp. 735610.
12. M. L. Anne, J. Keirsse, V. Nazabal, K. Hyodo, S. Inoue, C. Boussard-Pledel, H. Lhermite, J. Charrier, K. Yanakata, O. Loreal, J. Le Person, F. Colas, C. Compère, and B. Bureau, “Chalcogenide glass optical waveguides for infrared biosensing,” Sensors **9**(9), 7398–7411 (2009).
13. J. Charrier, M.-L. Brandily, H. Lhermite, K. Michel, B. Bureau, F. Verger, and V. Nazabal, “Evanescent wave optical micro-sensor based on chalcogenide glass,” Sensor. Actuat. B-Chem. **173**, 468–476 (2012).
14. J. J. Hu, V. Tarasov, A. Agarwal, L. Kimerling, N. Carlie, L. Petit, and K. Richardson, “Fabrication and testing of planar chalcogenide waveguide integrated microfluidic sensor,” Opt. Express **15**(5), 2307–2314 (2007).
15. M. Guignard, V. Nazabal, F. Smektala, J. L. Adam, O. Bohnke, C. Duverger, A. Moréac, H. Zeghlache, A. Kudlinski, G. Martinelli, and Y. Quiquempois, “Chalcogenide glasses based on germanium disulfide for second harmonic generation,” Adv. Funct. Mater. **17**(16), 3284–3294 (2007).
16. C. Monat, M. Spurny, C. Grillet, L. O’Faolain, T. F. Krauss, B. J. Eggleton, D. Bulla, S. Madden, and B. Luther-Davies, “Third-harmonic generation in slow-light chalcogenide glass photonic crystal waveguides,” Opt. Lett. **36**(15), 2818–2820 (2011).
17. C. C. Huang, D. W. Hewak, and J. V. Badding, “Deposition and characterization of germanium sulphide glass planar waveguides,” Opt. Express 12(11), 2501–2506 (2004).
18. J. M. Gonzalez-Leal, A. Ledesma, A. M. Bernal-Oliva, R. Prieto-Alcon, E. Marquez, J. A. Angel, and J. Carabe, “Optical properties of thin-film ternary $Ge_{10}As_{15}Se_{75}$ chalcogenide glasses,” Mater. Lett. **39**(4), 232–239 (1999).
19. L. Tichý, H. Ticha, P. Nagels, R. Callaerts, R. Mertens, and M. Vlcek, “Optical properties of amorphous As-Se and Ge-As-Se thin films,” Mater. Lett. 39(2), 122–128 (1999).
20. J. Charrier, M. L. Anne, H. Lhermite, V. Nazabal, J. P. Guin, F. Charpentier, T. Jouan, F. Henrio, D. Bosc, and J. L. Adam, “Sulphide GaxGe25-xSb10S65(x=0,5) sputtered films: Fabrication and optical characterizations of planar and rib optical waveguides,” J. Appl. Phys. 104(7), 073110 (2008).
21. V. Nazabal, F. Charpentier, J.-L. Adam, P. Nemec, H. Lhermite, M.-L. Brandily-Anne, J. Charrier, J.-P. Guin, and A. Moréac, “Sputtering and pulsed laser deposition for near- and mid-infrared applications: A comparative study of Ge25Sb10S65 and Ge25Sb10Se65 amorphous thin films,” Int. J. Appl. Ceram. Tec. 8(5), 990–1000 (2011).
22. M. Osawa and M. Ikeda, “Surface-enhanced infrared absorption of p-nitrobenzoic acid deposited on silver island films: contributions of electromagnetic and chemical mechanisms,” J. Phys. Chem. 95(24), 9914–9919 (1991).
23. J. M. Delgado, J. M. Orts, and A. Rodes, “A comparison between chemical and sputtering methods for preparing thin-film silver electrodes for in situ ATR-SEIRAS studies,” Electrochim. Acta 52(14), 4605–4613 (2007).
24. A. Pucci, F. Neubrech, D. Weber, S. Hong, T. Toury, and M. L. de la Chapelle, “Surface enhanced infrared spectroscopy using gold nanoantennas,” Phys. Status Solidi B 247(8), 2071–2074 (2010).
25. F. Neubrech, A. Pucci, T. W. Cornelius, S. Karim, A. García-Etxarri, and J. Aizpurua, “Resonant plasmonic and vibrational coupling in a tailored nanoantenna for infrared detection,” Phys. Rev. Lett. 101(15), 157403 (2008).
26. A. Hartstein, J. R. Kirtley, and J. C. Tsang, “Enhancement of the infrared absorption from molecular monolayers with thin metal overlayers,” Phys. Rev. Lett. 45(3), 201–204 (1980).
27. M. Osawa, “Dynamic processes in electrochemical reactions studied by surface-enhanced infrared absorption spectroscopy (SEIRAS),” Bull. Chem. Soc. Jpn. 70(12), 2861–2880 (1997).
28. T. Kamata, A. Kato, J. Umemura, and T. Takenaka, “Intensity enhancement of infrared attenuated total reflection spectra of stearic acid Langmuir-Blodgett monolayers with evaporated silver island films,” Langmuir 3(6), 1150–1154 (1987).
29. F. Verger, T. Pain, V. Nazabal, C. Boussard-Plédel, B. Bureau, F. Colas, E. Rinnert, K. Boukerma, C. Compère, M. Guilloux-Viry, S. Deputier, A. Perrin, and J. P. Guin, “Surface enhanced infrared absorption (SEIRA) spectroscopy using gold nanoparticles on As2S3 glass,” Sensor. Actuat. B-Chem. 175, 142–148 (2012).
30. J. Tauc, Amorphous and Liquid Semiconductors, J. Tauc ed. (Plenum, London, New York, 1974).
31. W. C. Tan, M. E. Solmaz, J. Gardner, R. Atkins, and C. Madsen, “Optical characterization of a-As2S3 thin films prepared by magnetron sputtering,” J. Appl. Phys. 107(3), 033524 (2010).

#197051 - $15.00 USD Received 3 Sep 2013; revised 8 Nov 2013; accepted 15 Nov 2013; published 22 Nov 2013

32. F. Charpentier, M. Dussauze, M. Cathelinaud, G. Delaizir, E. I. Kamitsos, J. L. Adam, B. Bureau, and V. Nazabal, "Aging process of photosensitive chalcogenide films deposited by electron beam deposition," J. Alloys Compd. 509(27), 7330–7336 (2011).
33. S. Sugai, "Stochastic random network model in Ge and Si chalcogenide glasses," Phys. Rev. B 35(3), 1345–1361 (1987).
34. L. Petit, N. Carlie, K. Richardson, Y. Guo, A. Schulte, B. Campbell, B. Ferreira, and S. Martin, "Effect of the substitution of S for Se on the structure of the glasses in the system Ge0.23Sb0.07S0.70-xSex," J. Phys. Chem. Solids 66(10), 1788–1794 (2005).
35. K. Jackson, A. Briley, S. Grossman, D. V. Porezag, and M. R. Pederson, "Raman-active modes of a-GeSe2 and a-GeS2: A first-principles study," Phys. Rev. B 60(22), R14985–R14989 (1999).
36. V. Nazabal, P. Nemec, A. M. Jurdyc, S. Zhang, F. Charpentier, H. Lhermite, J. Charrier, J. P. Guin, A. Moreac, M. Frumar, and J. L. Adam, "Optical waveguide based on amorphous Er3+-doped Ga-Ge-Sb-S(Se) pulsed laser deposited thin films," Thin Solid Films 518(17), 4941–4947 (2010).
37. K. Murase, T. Fukunaga, K. Yakushiji, T. Yoshimi, and I. Yunoki, "Investigation of stability of (Ge,Sn)-(S, or Se)4/2 cluster by vibrational-spectra," J. Non-Cryst. Solids 59–60, 883–886 (1983).
38. P. Němec, B. Frumarova, and M. Frumar, "Structure and properties of the pure and Pr3+-doped Ge25Ga5Se70 and Ge30Ga5Se65 glasses," J. Non-Cryst. Solids 270(1-3), 137–146 (2000).
39. Z. G. Ivanova, E. Cernoskova, V. S. Vassilev, and S. V. Boycheva, "Thermomechanical and structural characterization of GeSe2–Sb2Se3–ZnSe glasses," Mater. Lett. 57(5-6), 1025–1028 (2003).
40. J. H. Baeck, T. H. Kim, H. J. Choi, K. H. Jeong, and M. H. Cho, "Phase transformation through metastable structures in atomically controlled Se/Sb multilayers," J. Phys. Chem. C 115(27), 13462–13470 (2011).
41. R. Golovchak, O. Shpotyuk, M. Iovu, A. Kovalskiy, and H. Jain, "Topology and chemical order in AsxGexSe1-2x glasses: a high-resolution X-ray photoelectron spectroscopy study," J. Non-Cryst. Solids 357(19-20), 3454–3460 (2011).
42. D. C. Sati, A. Kovalskiy, R. Golovchak, and H. Jain, "Structure of SbxGe40-xSe60 glasses around 2.67 average coordination number," J. Non-Cryst. Solids 358(2), 163–167 (2012).
43. Y. Chen, X. Shen, R. Wang, G. Wanga, S. Dai, T. Xu, and Q. Nie, "Optical and structural properties of Ge–Sb–Se thin films fabricated by sputtering and thermal evaporation," J. Alloys Compd. 548, 155–160 (2013).
44. J. Siegel, O. Lyutakov, V. Rybka, Z. Kolská, and V. Svorčík, "Properties of gold nanostructures sputtered on glass," Nanoscale Res. Lett. 6(1), 96 (2011).
45. R. C. Munoz, G. Vidal, M. Mulsow, J. G. Lisoni, C. Arenas, A. Concha, F. Mora, R. Espejo, G. Kremer, L. Moraga, R. Esparza, and P. Haberle, "Surface roughness and surface-induced resistivity of gold films on mica: Application of quantitative scanning tunneling microscopy," Phys. Rev. B 62(7), 4686–4697 (2000).
46. M. Osawa, "Surface-enhanced infrared absorption," in Near-Field Optics and Surface Plasmon Polaritons (Springer, 2001), pp. 163–187.
47. R. F. Aroca, D. J. Ross, and C. Domingo, "Surface-enhanced infrared spectroscopy," Appl. Spectrosc. 58(11), 324–338 (2004).
48. Z. J. Zhang and T. Imae, "Study of surface-enhanced infrared spectroscopy - 1. Dependence of the enhancement on thickness of metal island films and structure of chemisorbed molecules," J. Colloid Interface Sci. 233(1), 99–106 (2001).
49. E. Bjerke, Amy, Griffiths, and R. Peter, Surface-enhanced infrared absorption spectroscopy of p-nitrothiophenol on vapor-deposited platinum films (Society for Applied Spectroscopy, Frederick, MD, USA, 2002).
50. P. M. Mendes, K. L. Christman, P. Parthasarathy, E. Schopf, J. Ouyang, Y. Yang, J. A. Preece, H. D. Maynard, Y. Chen, and J. F. Stoddart, "Electrochemically controllable conjugation of proteins on surfaces," Bioconjug. Chem. 18(6), 1919–1923 (2007).

1. Introduction

Since many years, the development of sensors is a great subject of research in the domain of optics [1]. An important step is the fabrication and the integration of optical components used for micro-optical sensors. The essential part of a sensing platform is the optical waveguide where the propagation of light or laser is required [2]. Planar or ridge waveguides are well suitable because of their light guidance and propagating capacity in a confined space. Glassy materials with high refractive index allow light control at very small scales and are suitable for high index contrast photonic devices [2]. Infrared spectroscopy is a powerful tool for detecting and determining the composition of complex samples. The mid-infrared range, between 4000 and 400 cm^{-1}, is very useful because most of the infrared signatures or "fingerprints" (fundamental transitions) of organic species and biomolecules are located in this window [3]. It is well known that this spectroscopic technique is simple, reliable, fast, cost-efficient and non-destructive. Infrared spectroscopy is used in various applications [4]

#197051 - $15.00 USD Received 3 Sep 2013; revised 8 Nov 2013; accepted 15 Nov 2013; published 22 Nov 2013

such as night vision, gas and biomolecules analyzing [5], thermography [6], agricultural and environmental [7] analysis, or quality control in food industry [8].

Chalcogenide glasses are promising sensors materials for the infrared spectral range [9, 10]. The main constituents of these vitreous materials are chalcogens elements (sulfur, selenium and tellurium); they are associated with other elements such as arsenic, germanium, gallium, or antimony for example. They can be drawn into optical fibers [11, 12] or fabricated as thin films (waveguides) [13, 14]. Other properties, specifically their extended optical transmission window from the visible to the far infrared (up to 20 µm), their high refractive index (usually between 2 and 3) or their nonlinear optical properties make them a class of optical materials with growing interest [15, 16]. The fabrication of chalcogenide thin films is usually carried out using chemical vapor deposition [17], thermal evaporation [18, 19], pulsed laser deposition, or radio-frequency sputtering [20, 21]. Since the thin films parameters, i.e. stoichiometric fidelity, structure, and optical properties can be affected by the deposition process, the choice of the deposition technique is crucial. Radio-frequency sputtering has been widely used due to its relative simplicity, easy control, often stoichiometric material transfer from target to substrate and large and multiple area coating [21].

One of the micro-optical sensors applications is the detection of molecules at low concentrations down to ppm or ppb level. To increase the sensitivity, the use of metallic nanoparticles is one of the promising solutions. Using various morphologies, thicknesses or inter-particles coupling [22–25], the infrared absorption of organic compounds can be strongly enhanced. This phenomenon is called surface enhanced infrared absorption (SEIRA) and was observed for the first time by Hartstein *et al.* [26]. Surface plasmons of metallic nanoparticles can be excited by the electric field of appropriate light; they can consequently create a stronger local electric field interacting with molecules by increasing their infrared absorption [27]. This phenomenon takes place in a nanometer scale, for molecules very close to metallic nanoparticles or adsorbed onto them [28]. In a previous study, we showed that chalcogenide glass bulk disks of As_2S_3 can be used as substrates for SEIRA spectroscopy [29].

The aim of this study is to contribute to develop an optical waveguide presenting a SEIRA effect. The first step is the fabrication of amorphous chalcogenide thin films (As_2S_3 and $Ge_{25}Sb_{10}Se_{65}$) by radio frequency (RF) sputtering and to investigate their physical-chemical properties. Once the deposition mastered and the optical, structural, morphological, or topographical characteristic better known, gold nanoparticles were deposited onto thin films by direct current (DC) sputtering to evaluate SEIRA spectroscopy of prepared planar waveguide structures.

2. Materials and experimental methods

2.1 Synthesis of glass target

A conventional method of melting and quenching was used to prepare the chalcogenide glass targets with the nominal composition of As_2S_3 and $Ge_{25}Sb_{10}Se_{65}$. Glassy targets were synthesized from high purity (5N) commercial elements (As, Ge, Sb, S, Se). Sulfur and selenium were pre-purified by dynamic as well as static distillation. The glass rods were obtained after overnight synthesis, using sealed amorphous silica ampules under vacuum, in a rocking furnace at 800 °C followed by quenching. The resulting glass rods were immediately annealed, at ~190 and ~310 °C for As_2S_3, and $Ge_{25}Sb_{10}Se_{65}$, respectively. Chalcogenide glasses with a diameter of 50 mm and thickness of 4 mm were obtained by slicing of the fabricated rods followed by polishing in order to be used as sputtering targets.

#197051 - $15.00 USD Received 3 Sep 2013; revised 8 Nov 2013; accepted 15 Nov 2013; published 22 Nov 2013

2.2 Thin films deposition by RF magnetron sputtering

The substrates used for the deposition of As_2S_3 and $Ge_{25}Sb_{10}Se_{65}$ thin films were chemically cleaned at room temperature with a detergent solution (surfactant) in an ultrasonic cleaner and then rinsed in distilled water and isopropanol in an ultrasonic bath. We used SiO_2/Si, CaF_2, Ge, ZnS, and $Ga_5Ge_{20}Sb_{10}S_{65}$ wafers as substrates. Chalcogenide thin films were deposited by RF magnetron sputtering under the following conditions. The working pressure and the Ar gas flow ranged from 5.10^{-3} to 5.10^{-2} mbar and 25-100 sccm, respectively; the sputtering power was stabilized at 40-60 W considering the semi-insulator character of the targets and the requirement of amorphous layers deposition. An off-axis substrate rotation was operated during the deposition process.

2.3 Gold films deposition by DC sputtering

Chalcogenide films used in this study contain sulfur or selenium, which allows a good adhesion of gold on the surface via Au-S (or Se) bonding; this is why no specific surface treatment of the chalcogenide films is required. After RF sputtering of chalcogenide films, gold thin films were directly deposited by DC sputtering. Gold was deposited at room temperature under pure Ar atmosphere with a pressure of 6.10^{-2} mbar. A 2.54 cm diameter gold target constituted of a pure gold foil (99% purity, 0.5 mm thick, Goodfellow) was fixed on the coaxial electrode.

2.4 Bulk and film characterization

The chemical composition of As_2S_3 and $Ge_{25}Sb_{10}Se_{65}$ bulk glasses and films was measured using a scanning electron microscope (SEM) with an energy-dispersive X-ray analyzer (JSM 6400-Oxford Link INCA, Buckinghamshire, UK). The SEM technique was also applied to observe the morphology of the thin films using a field emission gun SEM (JSM 6301F). Optical constants of fabricated thin films were extracted from transmittance spectra recorded with a visible-near-IR spectrophotometer (PerkinElmer, Shelton, CT, USA). Linear refractive indices spectral dependencies as well as optical band gap values were also obtained from the analysis of variable angle spectroscopic ellipsometry (VASE) data measured using two ellipsometers: first one (UV-near-IR) with an automatic rotating analyzer and second one (near-mid-IR) exploiting rotating compensator (both J. A. Woollam Co., Inc., Lincoln, NE, USA). The VASE measurements parameters are as follows: the spectral region of 300-10000 nm with wavelengths steps of 10 nm (UV-near-IR) or 20 nm (near-mid-IR) and angles of incidence of 50, 60, and 70°.

In the transparent spectral region of the material, the simple Cauchy dispersion relation is useful giving the refractive index:

$$n(\lambda) = A + B/\lambda^2 + C/\lambda^4 \quad (1)$$

where A, B, and C are fitted parameters and λ is the wavelength, setting the extinction coefficient $k = 0$ or assuming only weak Urbach's absorption. In case of absorption onset and strong absorption, the Cody-Lorentz model, which was already described and commented in details for the characterization of optical properties of amorphous chalcogenide films, was preferably used for the analysis of ellipsometric data.

The effective refractive indices of the propagation modes in the RF sputtered films were measured using the laser beam wavelengths of 633, 825, 1311, and 1551 nm (Metricon 2010 instrument, Pennington, NJ, USA), thus far enough from fundamental absorption of studied materials in order not to affect the determination of the refractive index. The mentioned wavelengths were used to excite the TE and TM modes inside the chalcogenide slab waveguides by means of the prism coupling technique. This M-lines technique can give an accurate measurement of the refractive index with a routine index accuracy of ± 0.0005

#197051 - $15.00 USD Received 3 Sep 2013; revised 8 Nov 2013; accepted 15 Nov 2013; published 22 Nov 2013

useful to validate the model used for VASE data simulation of amorphous chalcogenide films under study. A rutile prism was used for guaranteeing coupling with sputtered sulphide films while the silicon prism was selected for sputtered selenide films (1311 and 1551 nm), which present a larger refractive index.

2.5 Photolithography

First, the straight line patterns are defined on a SiO_2/Si substrate using photolithography (UV insulation through a waveguide optical mask and development of a photoresist layer). A gold film is deposited all over the patterned substrate. The photoresist is then removed with acetone, leaving part of the film which was deposited directly on the substrate. Then, the gold strips thickness is measured with a P6 stylus KLA-Tencor profilometer. The accuracy of the profilometry thickness determination is better than 1 nm. An estimate of an order of magnitude of the conductivity is determined by a simple electrical measurement on a gold strip. A 2-point probes station is used to measure the voltage drop (V) across the resistance (R) of the gold line when a current (I) is flowing between the two probes. Then according to Ohm's law

$$V = R.I. \tag{2}$$

The resistivity of the gold layer (ρ) is obtained by

$$\rho = l / R.l / s, \tag{3}$$

where *l* is the distance between the two probes, and *s* is the cross section of the gold line.

2.6 Raman spectroscopy

Raman scattering spectra were measured at room temperature using an HR800 (Horiba-Jobin-Yvon SAS, Villeneuve d'Ascq, France) micro-Raman spectrophotometer with a 785 nm laser diode as the excitation source. To avoid photoinduced phenomena, optical density filters have been used to reduce the laser power focused on the sample.

2.7 X-ray reflectometry and x-ray photoelectron spectroscopy

X-ray reflectometry (XRR) analyses were performed using a 4-circle high resolution diffractometer (D8 DISCOVER Bruker AXS, Karlsruhe, Germany), equipped with a parallel beam Cu $K\alpha_1$ radiation and operated in θ-2θ geometry. The measurements were recorded within the angular range of 0-6° (2θ) using a knife-edge located at 80 µm from the sample surface. The XRR scans were analyzed using the Bruker LEPTOS 6.02 software package (Bruker AXS, Karlsruhe, Germany) for modeling and fitting the thickness, density, and roughness.

A Kratos Axis Ultra X-ray Photoelectron Spectrometer was used to characterize the top surface of Ge-Sb-Se films using monochromatic Al Kα X-rays (1486.6 eV, 12 kV – 20 mA). Survey scans were recorded over the entire binding energy (BE) range using the constant pass energy of 80 eV and energy steps of 500 meV. Specific scans were selected over the core level photoelectron peaks ($Ge2p_{3/2}$, Sb3d-O1s Se3d, Sb4d-Ge3d) using the constant pass energy of 20 eV and energy steps of 100 meV. The other settings of the analyzer were those corresponding to the so called "Hybrid/Slot" mode in which the magnetic lens located below the sample holder is activated, and the analyzed area is typically 700x300 μm^2. Surface charging from photoelectron emission was neutralized using the built-in system, which combines a low energy (2.5 V extraction voltage) electron flood gun and the magnetic lens. The analysis was made at 0, 45, 60, and 70° take off angles with respect to the normal to the sample surface. The binding energy scale was calibrated using an internal reference. An oxygen atomic percentage of about 15% was observed, which corresponds to a weak surface oxidation and atmospheric contamination, whereas the residual carbon contamination could

#197051 - $15.00 USD Received 3 Sep 2013; revised 8 Nov 2013; accepted 15 Nov 2013; published 22 Nov 2013

not be estimated since the C1s core level overlaps with the Se $L_3M_{23}M_{45}$ Auger transition. The fitted peaks of the experimental curves are defined by a combination of Gaussian (70%) and Lorentzian (30%) contributions. In this work, the analysis of the Ge 2p core level spectrum was not taken into consideration simply because it should contain identical information as the Ge3d one; however, it does not correspond to the same probed depth compared to the Ge 3d core level, with a factor of about 4 times lower. We therefore focus our attention on 3d and 4d levels (Ge, Sb and Se). Each 3d (Ge, Se and Sb) and 4d (Sb) core-level spectrum is constituted of $3d_{5/2}$ and $3d_{3/2}$ spin orbit doublets.

2.8 Atomic force microscopy

Chalcogenide and gold thin films morphology and thickness were investigated by atomic force microscopy (AFM, Dimension 3100, Nanoscope V, Digital Instruments, Santa Barbara, CA, USA). Tapping mode imaging was used with a scanning mode area varying from 1 µm x 1 µm, and a doped silicon tip (BS-TAP300Al) with an average radius < 10 nm, and a resonant frequency of 300 kHz. AFM was calibrated with 10.3 µm grid pitches of 200 and 23 nm depths. For low roughness surface, Si atomic steps (0.314 nm, Si (111)) were used to calibrate the z-axis.

2.9 Surface enhanced infrared absorption spectroscopy effect

To evaluate the SEIRA effect and for a simple measurement in a transmission mode, Ge-Sb-Se thin films were deposited on substrates transparent in the IR spectral region ($Ga_5Ge_{20}Sb_{10}S_{65}$, Ge, and ZnS wafers). The thicknesses of the RF sputtered Ge-Sb-Se films are between 1.0 and 3.8 µm; SEIRA tests were performed on layers of 1 µm and 3-4 µm in order to evaluate the films resistance against gold deposition and functionalization treatments. As_2S_3 thin films could not be used for measuring the SEIRA effect due to relatively fast photo-crystallization observed at the surface. The fabrication of $Ge_{25}Sb_{10}Se_{65}$ sputtered films was then optimized considering the optimum deposition parameters (Ar pressure and power) in order to obtain a low surface roughness enabling an efficient deposition of gold nanoparticles at the surface of the selenide planar waveguide. The self-assembled monolayer of 4-nitrothiophenol (technical grade, Sigma-Aldrich) was prepared by soaking the gold-coated substrate in 20 mL of a 6.5×10^{-5} M aqueous solution of 4-nitrothiophenol for 15 hours at room temperature, then rinsed with ethanol and dried under a dry nitrogen flow. Thiol compounds are well known and used for gold surface functionalization since their molecules can be adsorbed onto a gold surface forming a monolayer via Au-S bonding.

The SEIRA spectra of 4-nitrothiophenol self-assembled on fabricated structures were recorded with an FTIR Thermo Nicolet spectrometer in a transmission mode, using a DTGS detector, with a resolution of 4 cm^{-1}; 256 scans were collected. The background spectrum of atmosphere was measured as a single beam and was used as a reference. A baseline correction was performed to eliminate the absorption of the substrate covered by gold nanoparticles in order to show the absorption of 4-nitrothiophenol only.

3. Results and discussion

3.1 Thin films of As_2S_3

As encouraging results were obtained in preliminary SEIRA tests on sulphide glass [29], the development of a planar waveguide by means of sputtering deposition of As_2S_3 bulk glasses was firstly investigated. The chemical composition of As_2S_3 bulk glasses and corresponding thin film are presented in Table 1.

#197051 - $15.00 USD Received 3 Sep 2013; revised 8 Nov 2013; accepted 15 Nov 2013; published 22 Nov 2013

Table 1. Chemical composition (± 0.5 at. %) of As_2S_3 bulk glass and sputtered thin film, refractive index (± 0.0005) of As_2S_3 sputtered thin film of about 1.5 µm thickness and corresponding Cauchy dispersion relation.

Elements	Theoretical [at. %]	Bulk [at. %]	Films [at. %]
As	40	36.3	42.0
S	60	63.7	58.0
Wavelength	633 nm	825 nm	1551 nm
Refractive index	2.5390	2.4501	2.3769
Cauchy dispersion	$n(\lambda) = 2.2895 + \frac{0.1227}{\lambda^2} - \frac{0.0091}{\lambda^4}$		

In comparison with nominal composition, sputtered thin films show a deficiency of 2% in chalcogen element (S) content; this shows a good reliability of used deposition method. The transmittance spectrum of the As_2S_3 sputtered film on a borosilicate substrate (BK7, Schott) is given in Fig. 1.

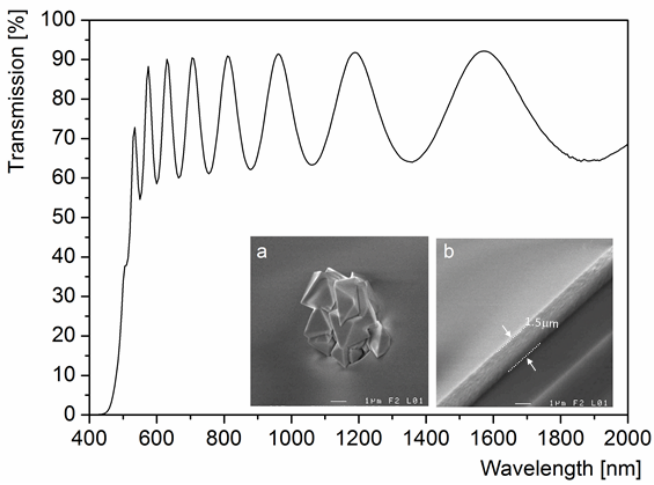

Fig. 1. Transmission curve of As_2S_3 sputtered thin film between 400 and 2000 nm. Insets show SEM pictures of As_2S_3 sputtered thin film after 48 hours ageing: a microcrystal on the film surface (a), film cross-section of about 1.5µm thickness (b).

The spectrum shows interference fringes which are typical for thin films with homogeneous thickness. Using measured transmittance spectra and following Tauc model [30], the optical band gap is calculated. Our results show that the band gap of RF sputtered As_2S_3 thin film is 2.30 ± 0.01 eV. This result is consistent with the value previously observed by Tan *et al*. [31]. Average refractive index (averaged from four sputtered thin films) values are presented in Table 1. Refractive index data are similar to Tan *et al*. [31]. Using refractive index values, the Cauchy dispersion relation can be expressed (Table 1). The thickness of As_2S_3 thin films is about 1.5 µm as estimated from scanning electron micrograph pictures (Fig. 1(b)). Examples of SEM pictures of RF sputtered As_2S_3 thin film, 48 hours after the deposition, are shown in the insets of Fig. 1. Figure 1(b) represents the cross-section micrograph; it shows that the layer is dense, homogeneous and does not contain column-like structures nor cracks. However, by the presence of some crystals on the surface (Fig. 1(a))

#197051 - $15.00 USD Received 3 Sep 2013; revised 8 Nov 2013; accepted 15 Nov 2013; published 22 Nov 2013

with the size of a few micrometers, we can indicate some ageing of the film. The formation of As_2O_3 crystals is attributed to the oxidation of arsenic by oxygen under ambient environment [32]. Such microcrystals affect the optical properties of the films by increasing optical losses and surface roughness. To avoid this problem, we decided to work further with more stable thin films even if our first measurements of SEIRA spectroscopy were performed using bulk As_2S_3 glasses [29]. We chose the Ge-Sb-Se system for several reasons. Firstly, antimony lowers the surface oxidation and the formation of crystals. Secondly, by introducing selenium instead of sulfur, the optical transparency of chalcogenide materials is extended further in the IR spectral range. We have also designed, developed and demonstrated evanescent field waveguides based on selenide films with microfluidic channels with optical losses of 0.4 dB/cm (at 1.55 μm) suitable for near-IR and mid-IR spectral range [13]. Moreover, hybrid nanoparticle–microcavity-based plasmonic nanosensors with improved detection resolution and extended remote-sensing ability were also developed using RF sputtered selenide films [9]. These two optical devices encourage us to consider the Ge-Sb-Se system for the development of optical sensor based on the SEIRA effect.

3.2 Thin films of Ge-Sb-Se system

Thin films with $Ge_{25}Sb_{10}Se_{65}$ composition can be obtained by sputtering with good optical properties and low optical losses [21]. Using $Ge_{25}Sb_{10}Se_{65}$ target, we prepared a series of corresponding Ge-Sb-Se thin films at different sputtering parameters. Among them, we selected two different values of Ar pressure (Table 2) to study the influence of deposition conditions on composition and morphology.

The films thicknesses determined by SEM and VASE data analysis agree well together, with thicknesses of about 1 μm, corresponding to the sputtering rate ~9 nm/min depending on parameters of deposition (power, Ar pressure, Ar flux, substrate/target distance, magnetron efficiency). We note no major influence of the sputtering pressure on the presented (low) sputtering rate. Further, Table 2 shows that the composition of the sputtered thin films is relatively close to the nominal chemical composition of the target, particularly at the sputtering pressure of 5.10^{-2} mbar.

Table 2. RF sputtering parameters, chemical composition and thicknesses of $Ge_{25}Sb_{10}Se_{65}$ thin films.

Sample	1	2	3
Ar pressure [mbar]	5.10^{-3}	5.10^{-2}	5.10^{-3}
Power [W]	40	40	60
Sputtering rate (nm/min)	9	9	9
Real composition [%], ±0.5%	$Ge_{29.6}Sb_{9.4}Se_{61.0}$	$Ge_{24.7}Sb_{8.7}Se_{66.6}$	$Ge_{28.9}Sb_{11.6}Se_{59.5}$
Thickness by SEM [nm]	1100	1100	1000
Thickness by VASE [nm]; ±5 nm	1016	1112	997

The morphology of the Ge-Sb-Se layers, observed by SEM cross-sections (Fig. 2), seems to be strongly influenced by the sputtering pressure. At even higher pressures incident species lose energy and adhesion problems may occur leading to granular and less dense films. At first step, very small cluster (of about 1 nm) are formed on substrate at room temperature corresponding to the nucleation phase. If there is no strong connection between the atom and the surface, the condensed atom diffuses on the surface until it hangs on a small island or contributes to the creation of a new cluster, after collisions with other diffusing atoms giving well separated islands. There will be a beginning of formation of a continuous

#197051 - $15.00 USD Received 3 Sep 2013; revised 8 Nov 2013; accepted 15 Nov 2013; published 22 Nov 2013

layer after the islands have reached significant thicknesses. A coalescence phase involves the formation of islands and then, channels before leading to a continuous film. However, holes can persist. Most of the films, deposited at room temperature, are particularly in non-equilibrium state and can have an important amount of defects.

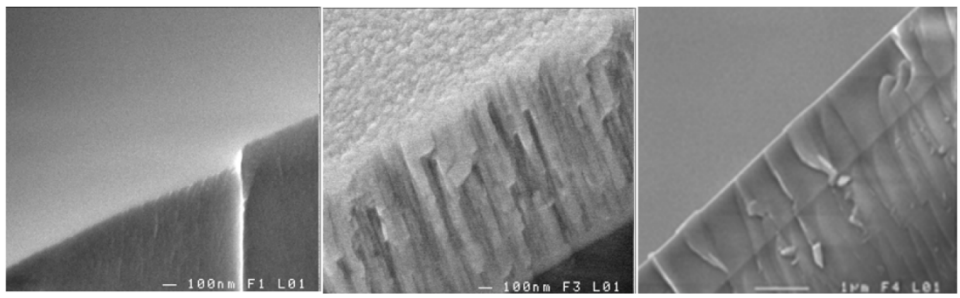

Fig. 2. SEM cross-section pictures of $Ge_{25}Sb_{10}Se_{65}$ thin films: 5.10^{-3} mbar, 40 W (a), 5.10^{-2} mbar, 40 W (b) and 5.10^{-3} mbar, 60 W (c).

Atoms arriving at the surface transfer their energy and can diffuse on the surface before being incorporated in favorable sites. As a general rule, at room temperature, few chemical elements can diffuse. When columns, between which exist cavities, are observed, this morphology is associated with a lack of surface diffusion. This leads to shadow effects inducing spikes generated by roughness substrate or initial nucleation. Similarly, a hole on the surface or a lack of small cluster leads to the formation of a cavity. It is probably the mechanisms that are brought into operation in the case of films deposited at higher pressure and ambient temperature.

Using Cauchy approach or Cody-Lorentz model, refractive index spectral dependences were extracted from VASE data analysis in the spectral range from 400 nm to 10 μm (Fig. 3). As the RF power does not seem to be a major factor influencing refractive index values, the power was set at 40 W for the rest of the study. One can conclude that a higher sputtering pressure results in a chemical composition closer to bulk glass target and substantially lower density films with columnar structure having consequently a lower refractive index. As expected, especially in the transparency region of the materials, refractive indices of selenide layers (Fig. 3) are higher than that of As_2S_3 thin films (Table 1) allowing the fabrication of photonic structures with high index contrast.

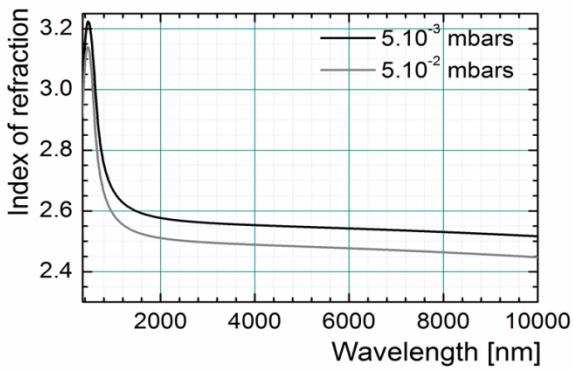

Fig. 3. Refractive index dispersion curves of $Ge_{25}Sb_{10}Se_{65}$ thin films determined by variable angle spectroscopic ellipsometry (VASE).

#197051 - $15.00 USD Received 3 Sep 2013; revised 8 Nov 2013; accepted 15 Nov 2013; published 22 Nov 2013

In order to identify and compare the structure, Raman spectra of various Ge-(Sb)-Se bulk glasses and two RF sputtered thin films (fabricated at different pressure) are presented in Fig. 4(a) and Fig. 4(b), respectively. Raman data of $GeSe_2$ bulk glass show two intense bands peaking at ~200 and ~215 cm^{-1} (Fig. 4(a)). These two bands are assigned to the symmetric stretching mode of $[GeSe_{4/2}]$ tetrahedra connected by the corners and to the vibrations of $[GeSe_{4/2}]$ tetrahedra connected by edges, respectively [21, 33–35]. An addition of antimony to $GeSe_2$ glasses leads to an intensity ratio decrease of the bands at ~200 compared to ~215 cm^{-1} (Fig. 4(a)), which indicates the slight increasing content of $[GeSe_{4/2}]$ tetrahedra connected by edges compared to those connected by corners. The second consequence of antimony addition is the appearance of a shoulder (band) at ~190 cm^{-1} assigned to Sb-Se bonds vibrations in $[SbSe_{3/2}]$ pyramids [36]. A band peaking at ~170 cm^{-1} (in Ge-Sb-Se glasses, its intensity decreases with increasing the content of antimony) can be connected with stretching modes of the Ge–Ge bonds in $[Ge_2Se_{6/2}]$ or $[Ge_{x/4}\text{-}Ge\text{-}Se_{(4-x)/2}]$ structural units as it is clearly observed in $Ge_{38}Se_{62}$ presenting a deficit in selenium (Fig. 4(a)).

Finally, a broad and low intensity feature of recorded Raman spectra is located in the region of 250-330 cm^{-1}. This broad band is probably formed by the overlap of several individual bands, which could be assigned to i) Se-Se stretching mode at the outrigger (~245 cm^{-1}), ii) Se-Se bonds (in dimers or less probably in short chains) vibrations (~265 cm^{-1}), iii) Ge-Ge bonds vibrations (in $Ge_x\mathbf{Ge}Se_{4-x}$, x = 1,2,3,4 structural units) similarly to amorphous germanium (~270 cm^{-1}), iv) F_2 asymmetric vibration modes of $[GeSe_{4/2}]$ tetrahedra (~300 cm^{-1}) [37, 38].

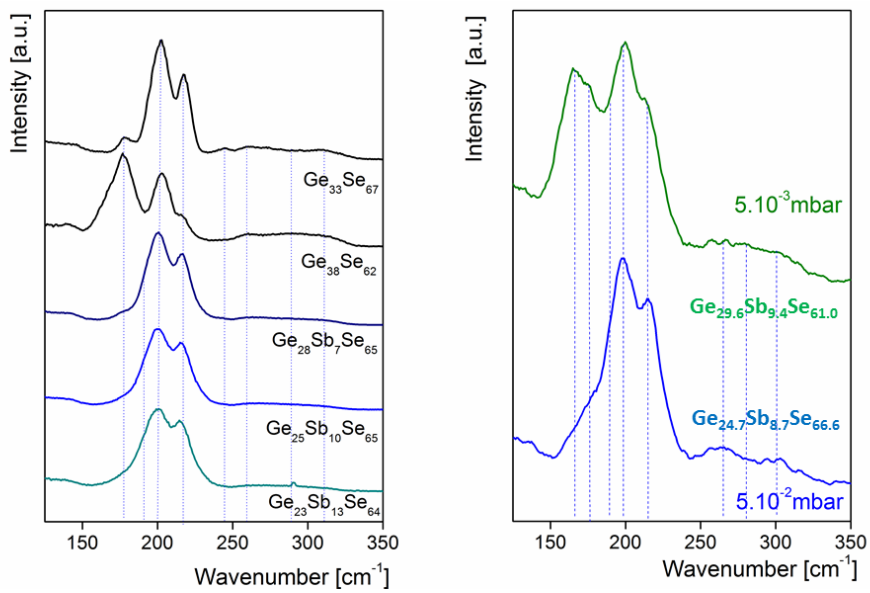

Fig. 4. Raman scattering spectra of Ge-(Sb)-Se bulk glasses (a, left) and sputtered thin films (b, right). Note that chemical compositions shown on left panel are theoretical ones.

Regarding thin films (Fig. 4(b)), at a lower pressure of 5.10^{-3} mbar, the band at ~165-175 cm^{-1} becomes more intense. The amplitude of the band at ~270 cm^{-1} also increases but the increase is lower. These results identify the presence of more Ge-Ge bonds forming $[Ge_{x/4}GeSe_{(4-x)/2}]$ or $[Ge_2Se_{6/2}]$ entities at the expense of $[GeSe_{4/2}]$ entities [21]. The presence of Sb-Sb bonds in $[SbSe_{(3-y)}(Ge,Sb)_y]$ entities cannot be clearly confirmed by Raman spectroscopy data due to band overlaps in the range of 150-180 cm^{-1} [39, 40]. Nevertheless, such a large band seems to be formed by two components (165 cm^{-1} and 175 cm^{-1}) likely associated to the vibration of Ge-Ge entities similar to the broad and asymmetric band in case

#197051 - $15.00 USD Received 3 Sep 2013; revised 8 Nov 2013; accepted 15 Nov 2013; published 22 Nov 2013

of $Ge_{38}Se_{62}$ bulk glass (Fig. 4(a)) with an additional contribution of Sb-(Sb,Ge) entities at 165 cm^{-1}. The intensity ratio of the bands at ~200 and 215 cm^{-1} is slightly different at a lower pressure; this qualitatively means that [$GeSe_{4/2}$] tetrahedra are connected by edges to a less extent [21, 33–35]. This analysis is basically analogous to that of glass presenting a comparable selenium deficit (Fig. 4(a)). Finally, Raman data show that the increase in the sputtering pressure leads to a film structure closer to similar bulk glass composition ($Ge_{25}Sb_{10}Se_{65}$) even if defects like Ge-Ge, Sb-(Ge,Sb) and Se-Se entities seem to be slightly more present.

X-ray photoelectron spectroscopy is used to describe bonding arrangement at the surface of Ge-Sb-Se layers, which could interact with sputtered golden films and influence the formation of golden nanoparticles. XPS data analysis is illustrated in Figs. 5(a)-(h). Concerning the XPS analysis of sputtered Ge-Sb-Se films, the agreement between the chemical composition determined by XPS and EDS is quite coherent as evidenced by the calculated [Ge]/[Sb] and [Se]/[Ge + Sb] ratio for the two sputtered films (Table 3).

The structure of Sb 4d Ge 3d core level bands is relatively complex with the overlapping of the peaks. It should be noticed that Sb 4d and Ge 3d core levels spectra reflect the variation of Ge/Sb ratio analyzed by EDS regarding to the pressure variation. In order to take into account the presence of SbO_x and GeO_x which are observed within the Sb3d and $Ge2p_{3/2}$ XPS data, it is necessary to add corresponding components for the XPS spectra curve fitting (Fig. 5(a) and 5(b), Table 3).

For the two films deposited at two different pressure, the presence of (Ge, Sb)-**Sb**-Se_2 and (Ge, Sb)-**Ge**-Se_3 species is observed. These homopolar bonds have also been demonstrated in publications concerning XPS of selenide glass [41, 42]. The proportion of (Ge, Sb)-**Sb**-Se_2 and (Ge, Sb)-**Ge**-Se_3 species is about 5.4 at.% and 1.7 at.% (for 5.10^{-3} mbars) and 2.1 at.% and 1.0 at.% (for 5.10^{-2} mbars) considering the atomic chemical composition obtained by XPS. This finding is in agreement with the Raman spectra recorded for the two films where vibrational modes related to depicted entities are present at ~165-175 cm^{-1}, in higher proportion in case of the film deposited at lower pressure. Nevertheless, it seems that the relative proportion of (Ge, Sb)-Sb-Se_2 and (Ge, Sb)-Ge-Se_3 entities differs between the XPS and Raman analyses. However, one should bear in mind that no real quantitative evaluation can be done from Raman scattering spectroscopy. The scattering efficiency might be really different for entities containing Ge-Ge or Sb-(Sb, Ge) bonds compare to [$GeSe_{4/2}$] tetrahedra distorting the perception of their relative quantities. The probed sample volume is also far from being the same for the two characterization techniques. In the case of XPS, characterizing first ten nanometers of the film surface, the analyses are certainly more influenced by surface oxidation and/or oxygen adsorption, while Raman spectroscopy gives average structural information including the surface as well as the volume of the film. In any case, XPS and Raman techniques demonstrated consistent trends regarding the presence and amount of homopolar bonds in accordance with the respective composition of the two films.

Two ($3d_{5/2}$ and $3d_{3/2}$) doublets are necessary to fit correctly the experimental Se 3d curve (Fig. 5(e) and 5(f)). Typically, Ge,Sb–**Se**–Ge,Sb entities are expected to be present in the glass network of sputtered films and located at similar chemical shifts due to comparable electronegativities of Ge (2.01) and Sb (2.05) atoms [41–43].

#197051 - $15.00 USD Received 3 Sep 2013; revised 8 Nov 2013; accepted 15 Nov 2013; published 22 Nov 2013

Table 3. Binding energy (BE, eV), full width at half maximum (FWHM, eV) and relative area (%) of the different components used for the fitting of Se $3d_{5/2}$, Ge $3d_{5/2}$ and Sb $4d_{5/2}$, Sb $3d_{5/2}$ core level spectra; [Se/(Ge + Sb)] and [Ge/Sb] composition ratio obtained experimentally by XPS compared to those obtained by EDS analysis.

Core Level	Species	5.10^{-2}mbar			5.10^{-3}mbar		
		BE [eV]	FWHM	[%]	BE [eV]	FWHM	[%]
Se $3d_{5/2}$	Se-$(Ge,Sb)_2$ CS	52.48	0.97	71	52.38	0.91	87
	Se-Se-$(Ge,Sb)_2$	53.14	0.97	29	52.98	0.91	13
Ge $3d_{5/2}$	Ge-$(Se)_4$	30.43	0.85	85	30.35	0.85	80
	(Ge,Sb)-Ge-$(Se)_3$	29.85	0.85	9	29.75	0.85	17
	Ge-Ox	31.53	0.85	6	31.45	0.85	3
Sb $4d_{5/2}$	Sb-$(Se)_3$	32.75	0.82	73	32.77	0.85	81
	(Ge,Sb)-Sb-$(Se)_2$	32.50	0.82	9	32.31	0.85	17
	Sb-Ox	33.35	0.82	18	34.00	0.85	2
Sb $3d_{5/2}$	Sb-$(Se)_3$	528.93	1.00	91	528.93	1.08	88
	(Ge,Sb)-Sb-$(Se)_2$	528.35	1.00	2	528.53	1.08	7
	Sb-Ox	529.74	1.00	7	530.11	1.08	5
Composition ratio		XPS	XPS/EDS		XPS	XPS/EDS	
Se/(Ge+Sb)		1.83	0.92		1.46	0.94	
Ge/Sb		2.79	0.98		3.12	0.99	

For the two sputtered films, the curve fitting of the Se 3d ($3d_{5/2}$ and $3d_{3/2}$) doublet reveals the presence of a second type of selenium (Se 3d doublet) unlikely related to the presence of SeO_x (Fig. 5(e) and 5(f)). The presence of SeO_x is clearly observed within the spectra obtained for a different angle of incidence; particularly at 70° (for which the in-depth analysis is restricted to an extreme surface of 2-3 nm), the presence of such oxygen containing entities was revealed. It is often proposed that this second component is attributed to Se-**Se**-Ge,Sb entities [41–43]. The proportion of Se-**Se**-Ge,Sb entities, if it exists, is predictable, from Raman analysis and chemical composition, to be higher for the (5.10^{-2} mbar) film than the (5.10^{-3} mbar) film, which presents a deficit of about ~9% of Se taking into account the real film composition determined by XPS ($Ge_{30.7}Sb_{9.9}Se_{59.4}$). Thus, a different shape of the Se 3d core level spectrum between the two selenide films can therefore be expected. However, the relative proportion of Se-**Se**-Ge,Sb entities (29%, Table 3) in relation to the composition of the (5.10^{-2} mbar) film seems to be a little bit surprising due to the following reasons (Fig. 5(e)). The first point is that the "stoichiometric" composition cannot explain the [Se-**Se**-Ge,Sb]/[Ge,Sb–**Se**–Ge,Sb] ratio observed. Moreover, the added components such as (Ge, Sb)-**Sb**-Se_2 or (Ge, Sb)-**Ge**-Se_3 in 3d Sb and Ge, as well as 4d Sb spectra for allowing the fit to converge reasonably, are in total proportion of about 3.1 at.%. This is confirmed by Raman spectra analysis suggesting the presence of Ge,Sb-Ge,Sb entities in the volume of the film in probably low amount. M-M bonds could explain a larger relative proportion of Se-**Se**-Ge,Sb species compared to Ge,Sb–**Se**–Ge,Sb but most likely not in such great proportion. We can therefore legitimately wonder about the presence of an additional contribution to the XPS component attributed to Se-**Se**-Ge,Sb. We would propose that this

#197051 - $15.00 USD Received 3 Sep 2013; revised 8 Nov 2013; accepted 15 Nov 2013; published 22 Nov 2013

new component contains information not only on Se-**Se**-Ge,Sb species but also on Se involved in the formation of bridges to link the [$GeSe_{4/2}$] tetrahedra by edges. The electronic structure of Se could be affected by this specific edge sharing when compared to a corner sharing between two [$GeSe_{4/2}$] tetrahedra. A similar scheme was applied for Ge 3d core level, fitted with two types of components (corner sharing and edge sharing), for the Ge-Se system rich in selenium [41]. Since the proportion of related edge sharing [$GeSe_{4/2}$] entities increases in the case of 5.10^{-2} mbar film according to Raman spectra analysis (Fig. 4(b)), such an assumption seems to be reasonable.

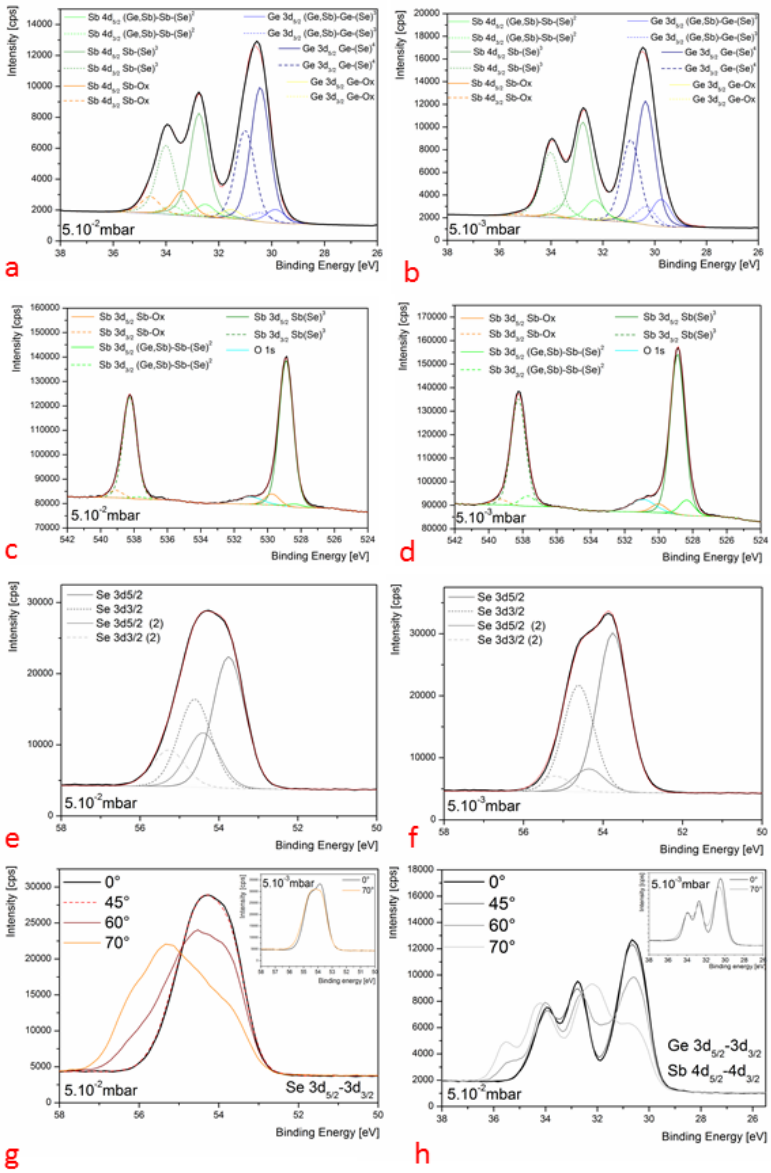

Fig. 5. XPS data of $Ge_{25}Sb_{10}Se_{65}$ sputtered films under 5.10^{-3} and 5.10^{-2} mbars of Ar: a) and b) curve fitting of Ge3d and Sb4d core level spectra; c and d) curve fitting of Sb3d core level spectra; e and f) curve fitting of Se3d core level spectra of sputtered films under 5.10^{-3} and 5.10^{-2} mbars of Ar, respectively; g) Se3d core level spectra and h) Ge3d and Sb4d core level spectra for normal, 45°, 60° and 70° take-off angle.

#197051 - $15.00 USD Received 3 Sep 2013; revised 8 Nov 2013; accepted 15 Nov 2013; published 22 Nov 2013

An oxidation effect onto the Ge-Sb-Se films is revealed with the take-off angle variation (angles: 0°, 45°, 60° and 70°) for the layers prepared under the Ar pressure of 5.10^{-2} mbar. However, the Sb 4d, Ge 3d and Se 3d core levels of the 5.10^{-3} mbar films show almost no variation. This is in agreement with the morphology of the films: the layers with higher porosity seem to be more affected by oxygen than denser films obtained at a lower pressure. Regarding the growing influence of the surface with the angle increase, it is not illogical to observe a more efficient oxidation in the case of the film realized at higher Ar pressure presenting a high roughness. However, we cannot exclude that different chemical composition and structure induced by the change of Ar pressure can play a role. There is no significant modification in [Ge]/[Sb] and [Se]/[Ge + Sb] ratio at the extreme surface (angle: 70°) compared to a deeper analysis of the film (angle: 0°). We thus speculate that at the extreme surface of the film (2-3 nm), the entities which are likely interacting with Au atoms during the gold sputtering deposition are constituted of selenide and oxide units (and probably mixed) without any important change of the composition within the first top 10 nm of the film.

3.3 Gold films deposition

Gold was sputtered on Ge-Sb-Se thin films (~1 µm thickness). The sputtering pressure of 5.10^{-3} mbar for the deposition of Ge-Sb-Se films was selected for different consideration. The first aim is to offer a really smooth surface affecting as less as possible the deposition of gold nanoparticles on the surface of the selenide planar waveguide. We noted that the columnar structure is affecting not only the roughness of the surface but also the thickness of the oxide layer at its surface (XPS analysis). The presence of this oxidized layer can affect the adhesion of gold nanoparticles which present a good affinity with chalcogenides but sensibly less good with oxide materials. The last point is the increase of optical loses of the planar waveguide not compatible with the development of an optical micro-sensor. In order to control the morphology of the gold thin films, the deposition of the gold nanoparticles was performed under different deposition parameter sets (Table 4).

Table 4. DC sputtering parameters and thicknesses of gold films by AFM.

Sample	1	2	3	4
Voltage [V]	1000	1000	1000	1200
Current intensity [mA]	0.44	0.44	0.44	0.62
Sputtering time [min]	15	5	2	1
Gold film thickness by AFM [nm]	34.0 ± 1.3	27.5 ± 6.8	13.5 ± 2.9	24.3 ± 3.0

SEM pictures of fabricated gold layers are given in Fig. 6. Here, it is possible to observe clearly the granular morphology of the film changing with the deposition time. The SEM and AFM pictures (Fig. 6 and Fig. 8(a)) show that gold films are made of dense gold nanoparticles. Gold films thicknesses measured by means of AFM are included in Table 4.

#197051 - $15.00 USD Received 3 Sep 2013; revised 8 Nov 2013; accepted 15 Nov 2013; published 22 Nov 2013

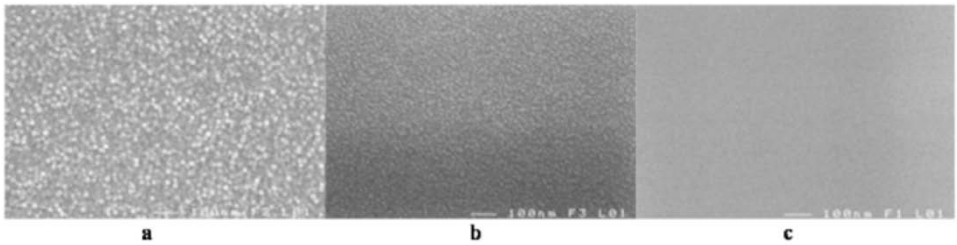

Fig. 6. SEM pictures (x 100 000) of gold films sputtered on $Ge_{25}Sb_{10}Se_{65}$ sputtered film: 1000 V, 0.44 mA, 15 min. (a), 5 min. (b), 2 min. (c).

The layers present thicknesses ranging from 13 to 34 nm depending on the deposition conditions. By decreasing the sputtering time down to 5 min (Fig. 6(b)) and 2 min (Fig. 6(c)), gold films seem to be less dense, loosing continuous character. The corresponding thickness decreases accordingly with the sputtering time from 27 nm (5 min deposition) to 13 nm (2 min deposition), which is in agreement with literature data [44].

Figure 7 illustrates experimental and simulated X-ray reflectometry (XRR) curves of $Ge_{29.6}Sb_{9.4}Se_{61.0}$ film (inset) and gold thin film deposited on $Ge_{29.6}Sb_{9.4}Se_{61.0}$ film by DC sputtering. The plateau length and the oscillation width of the curve are related to the density and the thickness of the layer, respectively. The oscillation amplitude and the tail of the curve are linked to the roughness of the layer and the substrate, respectively. Firstly, an XRR study was conducted on a thin layer of $Ge_{29.6}Sb_{9.4}Se_{61.0}$ deposited on Si substrate to determine the density of the selenide film. The structural model for the refinement chosen consists of the layer on Si substrate, regardless of a possible layer of native SiO_2 interface. Close and shallow oscillations are characteristic of a relatively thick layer (regarding X-ray reflectometry) with a low roughness; the refinement of those parameters is difficult and leads to relatively significant uncertainties in the obtained values (thickness 150 ± 10 nm, roughness 0.7 ± 0.1 nm, and density 4.5 ± 0.1 g/cm^3). Simulation attempts with an interface layer (SiO_2) did not lead to significant changes of the results. Using the estimated density of the single $Ge_{25}Sb_{10}Se_{65}$ film, Au/$Ge_{25}Sb_{10}Se_{65}$/SiO_2/Si hetero-structure was studied with the aim of determining the gold film thickness. $Ge_{29.6}Sb_{9.4}Se_{61.0}$ film having a thickness of ~1 µm (in order not to take into account the lower layers in the fit) assimilates the amorphous film as substrate.

There is a good correlation between the experimental curve and the simulated curve for the plateau which is characteristic of the density of the gold film. The density obtained (17.6 ± 0.2 g/cm^3) is, however, lower than the theoretical density of the bulk gold (19.1 g/cm^3). This discrepancy may be caused either by a discontinuous nature of the layer or some gradient of oxygen in the gold layer. Considering the oscillations width, a good fit is also obtained between the experimental and simulated curves (Fig. 7), which allows the determination of the thickness of the gold layer (22 ± 1 nm). On the other hand, there is no perfect overlap between the simulated curve and the experimental curve for the oscillations depth (gold roughness), and also for angle values greater than 4° (2θ). This can be attributed to the presence of an interface layer between the gold and selenide films establishing a connection with the XPS analyses.

#197051 - $15.00 USD Received 3 Sep 2013; revised 8 Nov 2013; accepted 15 Nov 2013; published 22 Nov 2013

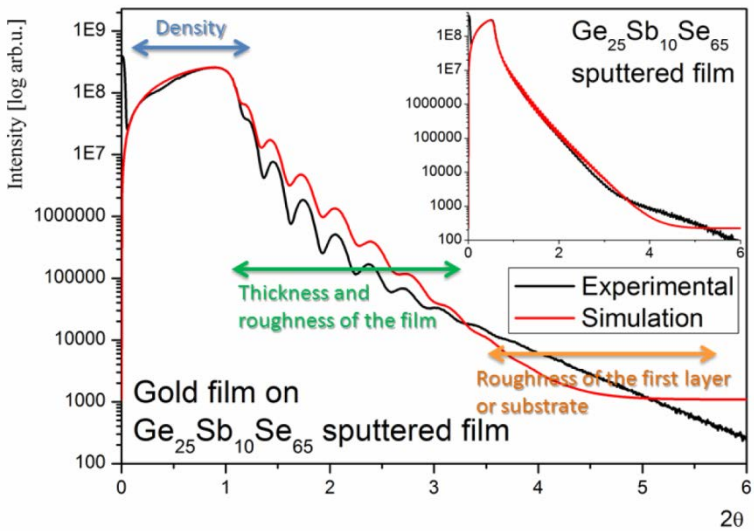

Fig. 7. X-ray reflectometry experimental and simulated data of $Ge_{29.6}Sb_{9.4}Se_{61.0}$ film (inset) and gold thin film deposited by DC sputtering on $Ge_{29.6}Sb_{9.4}Se_{61.0}$ film.

The conductivity measurements were performed in order to evaluate when nanoparticles stop forming a continuous films. The gold strip was fabricated using gold DC sputtering through a lift-off pattern (Fig. 8(b)). Obtained results show the resistivity value of ~8.10^{-6} Ω.cm for a 15 min (1000 V, 0.44 mA) sputtered continuous gold film and increases following the decrease of gold film thickness. This value is qualitatively consistent with the resistivity ρ_{Au} of Au bulk ($2.2.10^{-6}$ Ω.cm [45]) taking into account contact resistance of a tip and distance imprecision between the two tips. For the thinner (discontinuous) gold film (1000 V, 0.44 mA, 2 min), the resistivity increases up to 4 Ω.cm reaching the value of a semiconducting material. For the gold deposition condition (1200 V, 0.62 mA, 1 min), the layer is also discontinuous.

3.4 Demonstration of SEIRA effect on chalcogenide thin films

Surface enhanced infrared absorption (SEIRA) was observed for the first time in 1980 by Hartstein *et al.* [26]. The enhancement is commonly explained by electromagnetism mechanism through the generation of surface plasmons in the mid-IR spectral range [46]. Most of the SEIRA active substrates are made of nanoparticles very densely packed deposited on crystal substrates (CaF_2, ZnS, ZnSe, Ge, Si). They can be fabricated by different processes: electrochemically roughed electrodes, deposition by sputtering, thermal evaporation or colloid chemistry. These different substrates have demonstrated enhancement factors between 10 and 100 [46]. For the last decades several groups found various applications for surface enhancement phenomenon [47]. In a previous study, we successfully demonstrated SEIRA spectroscopy using gold nanoparticles deposited on surface of As_2S_3 bulk glass which can be shaped into integrated optical devices devoted to mid-IR [29]. For SEIRA spectroscopy, thin discontinuous gold films are required on chalcogenide optical waveguide. Thus, suitable DC sputtering parameters were selected to produce a discontinuous gold film on $Ge_{29.6}Sb_{9.4}Se_{61.0}$ thin film in order to increase the intensity of 4-nitrothiophenol absorption.

An example of AFM scan of $Ge_{29.6}Sb_{9.4}Se_{61.0}$ thin film after gold deposition is given in Fig. 8(a). From Fig. 8(a), one can note that the surface of the structure appears rough, and some gold nanoparticles with a diameter of less than 20 nm are observed. The optimal

#197051 - $15.00 USD Received 3 Sep 2013; revised 8 Nov 2013; accepted 15 Nov 2013; published 22 Nov 2013

thickness of a gold island film on As_2S_3 bulk glass is 16 ± 1 nm because they become nearly continuous with the increase of thickness [29].

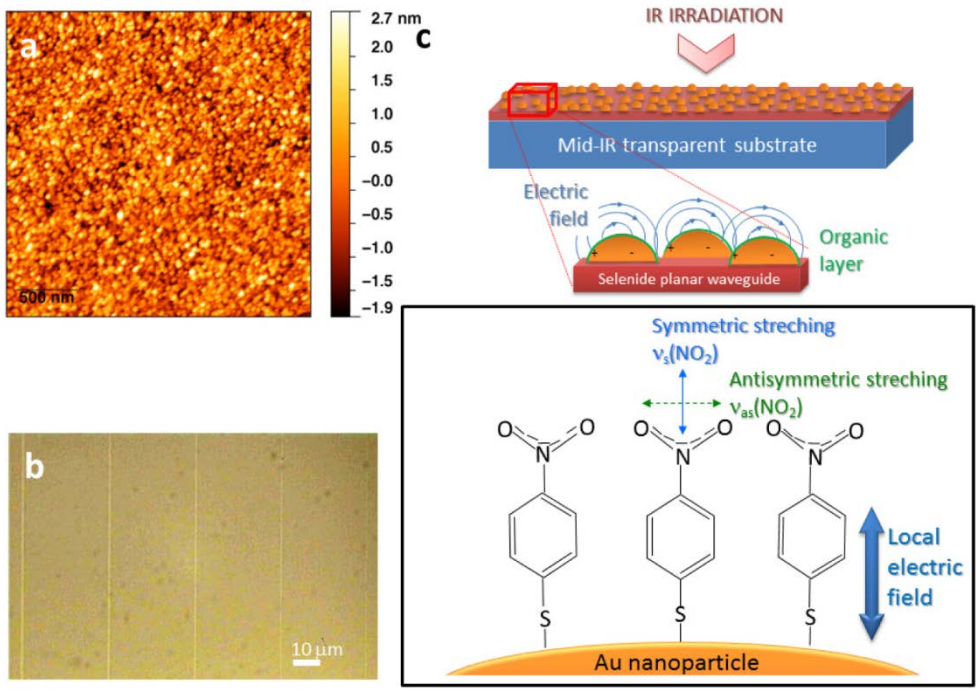

Fig. 8. a) AFM picture of the $Ge_{29.6}Sb_{9.4}Se_{61.0}$ thin film surface after gold deposition of nanoparticles (1000 V, 0.44 mA, 2 min); b) Optical microscopy picture of sputtered gold strips obtained by lift-off photolithography technique; c) Schematic representation of SEIRA optical component and expected configuration of 4-nitrothiophenol on gold nanoparticles.

To assess SEIRA effect, we used a self-assembled monolayer of 4-nitrothiophenol. The infrared spectra of 4-nitrothiophenol self-assembled monolayers, as well as randomly oriented ones, are well known. Figure 9(a) shows the infrared transmission spectrum of randomly oriented 4-nitrothiophenol on mid-IR transparent bulk substrate. According to work of Zhang and Imae [48], the strongest bands located at 1336 and 1512 cm^{-1} are attributed to NO_2 symmetric and antisymmetric stretching modes, respectively. Since the local electric field lines generated by surface plasmons are normal to the gold surface at each point, i.e. around gold nanoparticles, only groups with their dipole moments parallel to the field lines are enhanced (Fig. 8(c)). The NO_2 symmetric stretching mode of the 4-nitrothiophenol monolayer is SEIRA active, whereas the antisymmetric one is inactive. In contrast, the infrared transmission spectrum of randomly oriented 4-nitrothiophenol (Fig. 9(a)) shows both, symmetric and antisymmetric NO_2 stretching modes.

#197051 - $15.00 USD Received 3 Sep 2013; revised 8 Nov 2013; accepted 15 Nov 2013; published 22 Nov 2013

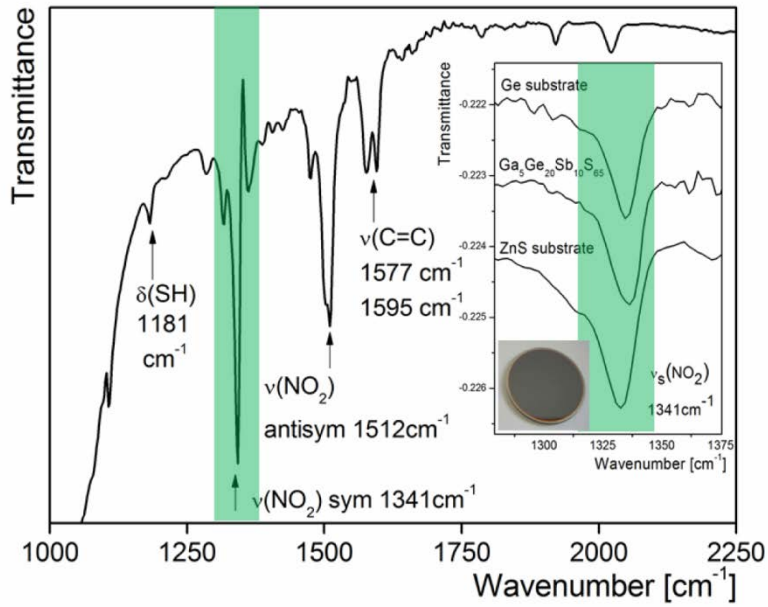

Fig. 9. a) Infrared spectrum of randomly oriented 4-nitrothiophenol on mid-IR transparent substrate and b) in inset: infrared transmission spectra of 4-nitrothiophenol monolayers on sputtered gold island (6.10^{-2} mbar, 1200 V, 0.62 mA, 70 s) onto $Ge_{25}Sb_{10}Se_{65}$ thin films deposited on various substrates (Ge, $Ga_5Ge_{20}Sb_{10}S_{65}$, ZnS).

Due to the depicted surface selection rules [49], we focused on the 1280-1375 cm^{-1} spectral region (Fig. 9(b)). The NO_2 symmetric stretching band at 1336 cm^{-1} is clearly detected with fabricated structures. The shift, about 5 cm^{-1}, is characteristic of the SEIRA effect due to the band asymmetry [49] observed without any baseline correction. Note that when using Ge-Sb-Se thin films, there is no absorption band (the decrease of the transmittance) at 1500 cm^{-1} attributed to CS_2 impurities which was observed when As_2S_3 glass was used [29]. The largest decrease of transmittance obtained at ~1336 cm^{-1} is 0.0021%, which is of the same order of magnitude as previously observed on As_2S_3 bulk glass (0.0072%). The nature of the substrate used (Ge, chalcogenide glass or ZnS) for the deposition of $Ge_{29.6}Sb_{9.4}Se_{61.0}$ thin film does not particularly influence neither the optical quality of the films nor their adhesion. The refractive indices and the dielectric constants are specific to each material and modify the plasmon resonance frequency. Simulations, by means of Mie theory in the case of a metallic gold nanosphere in homogeneous refractive index media, show that the position of the extinction band (absorption and diffusion) moves to the infrared range with an increase of refractive index. In the case of nanoantennas, Novotny formula also shows that when the effective index of surrounding medium increases, the position of the resonant frequency is also moved to higher wavelengths. Nevertheless, $Ge_{29.6}Sb_{9.4}Se_{61.0}$ film seems to be thick enough as the position of the absorption band of the NO_2 symmetric stretching mode is almost not modified by the specific characteristics of the substrates.

To evaluate the SEIRA enhancement factor, one possible way is to compare the infrared absorption intensity of the same amount of molecules without a gold film [22]. The decrease in the transmittance of $2.5.10^{-5}$ g of $Ge_{29.6}Sb_{9.4}Se_{61.0}$ of 4-nitrothiophenol randomly oriented is 0.029% (at ~1336 cm^{-1}). The analyzed amount of a self-assembled monolayer is calculated using the molecular density on gold [50], the molar mass, the area of the substrate covered by gold nanoparticles, the Avogadro's number, and the optical aperture of the sample holder.

#197051 - $15.00 USD Received 3 Sep 2013; revised 8 Nov 2013; accepted 15 Nov 2013; published 22 Nov 2013

Calculations show that the 4-nitrothiophenol layer represents $7.58.10^{-8}$ g. In this way, we found the chalcogenide thin films enhancement factor to be ~24 compared to ~82 in case of bulk chalcogenide glass. The decrease in the transmittance, related to the absorption of molecules, depends on the extinction coefficient of the discontinuous gold films [29], and so affects the enhancement factor. Our method of gold deposition could form some variations in the extinction coefficient of gold that explains observed slight differences of the absorption band at ~1336 cm^{-1} among different samples. Nevertheless, our results are similar to the work of Bjerke *et al*. [49] who studied the SEIRA of 4-nitrothiophenol on platinum island films.

4. Conclusion

Taking into consideration the development of micro-optic sensors allowing infrared absorption of organic compounds enhanced by surface plasmon effect, hetero structures combining gold nanoparticles and chalcogenide planar waveguides were manufactured and characterized. The radio-frequency magnetron sputtering technique was used for the preparation of single As_2S_3 and $Ge_{25}Sb_{10}Se_{65}$ amorphous chalcogenide films. To prepare gold nanoparticles on top of chalcogenide films, direct current sputtering was employed; the deposition parameters required to manufacture such metallic nanoparticles were optimized. $Ge_{25}Sb_{10}Se_{65}$ thin films were finally selected for their resistance to crystallization and/or ageing. Moreover, the selenide composition has the advantage of shifting the transparency further in the mid-IR but also can easily produce optical microstructured waveguides by photolithography and reaction ion etching. Higher sputtering pressure results in substantially lower density of selenide films with columnar structure having a lower refractive index. By the fitting of XPS data, we concluded that germanium, antimony, and selenium atoms form bonds with oxygen preferentially for the higher pressure (5.10^{-2} mbars) used during the sputtering deposition likely related with a columnar structure of the sputtered film. Due to their better properties, a pressure of 5.10^{-3} mbars was then selected to fabricate high quality selenide films and optical waveguides devoted to gold nanoparticles deposition. At shorter deposition times, gold layers are losing continuous character and form dense nanoparticles on the surface of the selenide film. For discontinuous gold layers, the resistivity increases reaching values of semiconducting material which tends to prove that the deposits obtained are not continuous but composed of nanoparticles. The surface enhanced infrared absorption spectroscopy of 4-nitrothiophenol self-assembled on fabricated Au nanoparticles deposited on Ge-Sb-Se optical waveguide was demonstrated. Fabricated Au/Ge-Sb-Se hetero-structures present ~24 enhancement factor for the detection of an NO_2 symmetric stretching band of 4-nitrothiophenol at 1336 cm^{-1} showing the applicability of selenide amorphous optical waveguide covered with discontinuous gold layers for the surface enhanced infrared absorption spectroscopy. Thus, these optical micro-sensors based on selenide films provide new opportunities for the detection of bio-chemical molecules in mid-IR spectral range and can wisely use the SEIRA effect to increase their sensitivity.

Acknowledgments

The University of Rennes 1, CNRS, IFREMER and Ministry of Education, Youth and Sports of the Czech Republic, Project CZ.1.07/2.3.00/30.0058, financially supported this work.

#197051 - $15.00 USD Received 3 Sep 2013; revised 8 Nov 2013; accepted 15 Nov 2013; published 22 Nov 2013